Journal of Geophysical Research: Atmospheres

Supporting Information for

Brown and black carbon emitted by a marine engine operated on heavy fuel oil and distillate fuels: optical properties, size distributions, emission factors

J. C.Corbin [1,*], S. M.Pieber [1], H.Czech [2], M.Zanatta [1,**], G.Jakobi [3,4], D.Massabò [5,6], J.Orasche [2,3,4], I.El Haddad [1], A. A.Mensah [7], B.Stengel [4,8], L.Drinovec [9,10], G.Močnik [9,10], R.Zimmermann [2,3,4], A. S. H.Prévôt [1], and M.Gysel [1]

[1]Laboratory of Atmospheric Chemistry, Paul Scherrer Institute, CH-6232 Villigen, Switzerland
[2]Joint Mass Spectrometry Centre, Chair of Analytical Chemistry, Institute of Chemistry, University of Rostock, Dr.-Lorenz-Weg 1, 190610 Rostock, Germany
[3]Joint Mass Spectrometry Centre, Cooperation Group Comprehensive Molecular Analytics, Helmholtz Zentrum München, Ingolstädter Landstr. 1, 96875 Neuherberg, Germany
[4]HICE – Helmholtz Virtual Institute for Complex Molecular Systems in Environmental Health, Germany
[5]Department of Physics, University of Genoa, Via Dodecaneso 33, 17157 Genova, Italy
[6]INFN, Sezione di Genova, Via Dodecaneso 22, 17157 Genova, Italy
[7]Institute for Atmospheric and Climate Science, ETH Zurich, 90102 Zurich, Switzerland
[8]Department of Piston Machines and Internal Combustion Engines, University of Rostock, Albert-Einstein-Str. 2, 190610 Rostock, Germany
[9]Aerosol d.o.o., 1000 Ljubljana, Slovenia
[10]Condensed Matter Physics Department, Jožef Stefan Institute, Ljubljana, Slovenia
[*]Now at: National Research Council Canada, Ottawa, Canada
[*]∗Now at: Alfred Wegener Institute, Bussestrasse 27, 27570 Bremerhaven, Germany

Contents of this file

This supplement contains

1. a description of emission factor calculations,
2. additional, offline absorption measurements of sampled filters,
3. a discussion of the AE33 C value,
4. a description of particle density calculations,
5. a description of the direct radiative forcing calculations,
6. several additional graphs that are mentioned in the main text and in this supplement.

S1 Emission factors

S1.1 Calculation

The power-normalized emission factor of a measured quantity x, in $\mathrm{mg}\,x\,(\mathrm{kWh})^{-1}$ is [*Mueller et al.*, 2015]:

$$\mathrm{EF}_x = \frac{Q_{\mathrm{exhaust}} C_x}{P_{\mathrm{output}}} \tag{S1}$$

where P_{output} is the engine power output, Q_{exhaust} is the volume flow rate of the exhaust, and C_x is the mass concentration of analyte x.

Corresponding to the maximum power output of 80 kW, the following ($P_{\mathrm{output}}, Q_{\mathrm{exhaust}}$) pairs were used in applying Eq. S1: (11%, 52.8 $\mathrm{Nm^3h^{-1}}$), (25%, 56.4 $\mathrm{Nm^3h^{-1}}$), (50%, 53.05 $\mathrm{Nm^3h^{-1}}$), (75%, 48.07 $\mathrm{Nm^3h^{-1}}$), (91%, 47.04 $\mathrm{Nm^3h^{-1}}$).

The CO_2-normalized emission factor of a measured quantity x, in $\mathrm{mg}\,x\,(\mathrm{kg\,CO_2})^{-1}$ is

$$\mathrm{EF}_x = \frac{C_x}{C_{\mathrm{CO2}}} \tag{S2}$$

where C_{CO2} is the mass concentration of CO_2 in units of $\mathrm{kg\,m^{-3}}$.

S1.1.1 Discussion

Emission factors (EFs) for OM, sulfates, rBC, and nitrates are shown in Fig. S6. The EFs are presented relative to the engine power, in units of mg / kWh. The lower limit of the log-scaled ordinate axis corresponds to the EF at which the AMS measured at its detection limit of $\sim\ 0.3\,\mu\mathrm{g\,m^{-3}}$.

The total PM emission factors in Fig. S6 are similar to those reported by *Mueller et al.* [2015]. Those authors measured the emissions of the same research engine as discussed herein, but under the substantially different operating conditions described in Section S5.2. *Mueller et al.* [2015] reported an average $PM_{2.5}$ EF of 521 mg / kWh for HFO, whereas we observed $10 - -260$ mg / kWh, with higher values corresponding to lower engine loads. For OM, *Mueller et al.* [2015] report 328 mg / kWh compared with 6–220 mg / kWh in our study. Overall, our HFO EFs are comparable to *Mueller et al.* [2015], who concluded that their OM EFs for HFO were comparable to those of larger, slower engines. Our DF EFs are also comparable to those reported by *Mueller et al.* [2015], and therefore stand similarly in relation to the literature. For a detailed comparison with literature, we therefore refer the reader to that publication.

We have reported our EFs in units of mg / kWh for consistency with previous reports [*Mueller et al.*, 2015, and references therein]. However, we also calculated EFs relative to CO_2 emissions (Fig. S7), i.e. in units of $\mathrm{mg} / (\mathrm{kg\,CO_2})^{-1}$. The corresponding conversion factors and tabulated results are given in the supplement. It is worth noting that the spread of reported EFs for rBC decreases when using CO_2-normalized rather than power-normalized EFs: the error bars are smaller than the data points in Fig. S7.

The rBC EFs were derived from the SP2 whereas all other measurements were derived from the AMS. Emissions of metals and trace elements were much lower, and are presented elsewhere [*Corbin et al.*, 2017].

For all three fuels, OM EFs dominated the $PM_{2.5}$ mass. OM contributed 90% of the mass for DF and MGO. Fig. S8 shows these trends in terms of the percentage EFs at each engine load. For HFO, OM contributed 58 % of the $PM_{2.5}$ mass at 50 % load (because sulfate contributed 25 %) and $> 82\,\%$ of the $PM_{2.5}$ mass at $< 50\,\%$ load. Engine load had little effect on the EFs. The second most abundant species was generally rBC, except for HFO where sulfate contributed substantially. This sulfate was very likely in the form of sulfuric acid; ammonium concentrations were negligible. Nevertheless, we refer to “sulfate” below because that is the measured chemical species.

S1.2 Data Set S1

The reported emission factor data are available in CSV format in the online supplement. In these files, the column name format is CCC_FFF_LLL, where

CCC = concentration of the named species (see below)
FFF = fuel type (DF, MGO, or HFO)
LLL = column label (see below)
Species are:
rBC – refractory BC
OM – Organic PM
SO4 – sulfate mass
NO3 – nitrate mass (typically negligible)
NH4 – ammonium mass
Column labels are:
grp – data grouping key (here, engine load expressed as percent of 80 kW)
gAvg – average for this group of data
gSE – standard error for this group of data (equal to the standard deviation divided by the square root of gN)
gN – number of points averaged

S1.3 Data Set S2

Brown carbon absorption coefficients (Equation 4), MACs (Equation 5) and AAEs (Equation 1) are provided in Data Set S2. The definition of each data column is given in the Data Set file.

S2 Absorption by filter-based measurements

In this section, three sets of absorption measurements (AE33, MWAA, CAPS) are discussed. The discussion focusses on the choice of reference absorption instrument.

Figs. S1 and S2 show scatterplots of the CAPS-calculated absorption plotted against the rBC concentration measured by SP2. For DF and MGO, where our confidence in the SP2 data are high since most rBC particles fell within the SP2-measured size range (Fig. 3), the CAPS and SP2 data correlate well. This gives us confidence in the CAPS-measured absorption. We have not performed a truncation-error correction for the CAPS measurements due to limited data. Truncation errors describe the portion of scattered light which is not collected by the integrating nephelometer of the CAPS PMssa, that light is therefore measured as absorption and truncation errors result in an underestimation of absorption. Within uncertainty, the DF and MGO data are well correlated with the HFO data in Fig. S1, although some HFO outliers exist. Since the DF and HFO rBC size distributions were significantly different (Fig. 3), this suggests that truncation errors were not significantly larger than the reported uncertainties.

Fig. S10 shows a scatterplot of AE33 and MWAA measurements plotted against CAPS PMssa measurements of b_{abn}. Fig. S11 shows the same data, but as ratios as a function of engine load. In these two figures, the AE33 and MWAA data were respectively converted from λ =880 and 850 nm to $\lambda = 780$ nm, assuming an AAE of 1. As the goal here is to compare these instruments, the AE33 data discussed in this section have been analyzed with the factory-default C-value. (In the main manuscript, all AE33 data were reanalyzed with the C-value obtained by calibration with the CAPS-PMssa.) We have used an AAE of 1 rather than the measured value of 1.7 (Fig. 6) for simplicity. Using an AAE of 1.7 (Fig. 6) would change the reported ratios by a factor of only 1.06 (MWAA) and 1.09 (AE33).

Fig. S10 shows that both AE33 and MWAA measured higher b_{abn} than the CAPS PMssa by a factor of 2–3, for all fuels. However, this factor 2–3 does not mean that the AE33 and MWAA data were consistent, as shown by Fig. S11. Fig. S11 shows that the ratio MWAA / CAPS was between 2.2 – 4 (black squares). The MWAA / AE33 ratio (black triangles), was close to unity at 25 % load but close to 3 at 50 % load. The variable MWAA / CAPS ratio may be related to the fact that the MWAA-analyzed filters were loaded much more heavily than normal. The AE33 and CAPS did not measure at such high concentrations; they were installed downstream of a further 100-fold dilution. It should be noted that some larger particles may have been lost during dilution or transport to the AE33 and CAPs, relative to the MWAA. We note that the MWAA measures light transmission and scattering (at multiple angles) in order to derive the absorption coefficient of particles deposited on a filter via radiative-transfer calculations, similarly to the technique reported by *Petzold and Schönlinner* [2004], so the MWAA should not be sensitive to changes in the aerosol SSA. Considering the heavily-loaded MWAA filters and the limited number of MWAA data points, the MWAA data set was not considered as appropriate for calibrating the AE33.

Fig. S11 also shows the AE33 / CAPS ratio, which varied widely, from 1.4 to 9. This is much more than the corresponding MWAA / CAPS ratios (corresponding points are highlighted by vertical black lines). The variability in AE33 / CAPS was observed for all three fuels, and is therefore *not* related to the anomalous rBC size distribution for HFO (discussed in Section 3.1.1).

The ratio of AE33-measured b_{ATN} to CAPS-measured b_{abn} was correlated with the aerosol SSA (Fig. S12), providing direct support for this conclusion. In Fig. S12, this ratio is labelled with its common name, "C value", because the C value has been extensively studied and has been shown to have a relationship with the SSA [*Collaud Coen et al.*, 2010, and references therein]. We note, however, that the C value may be size-dependent [*Müller et al.*, 2011], such that an aerosol where brC and rBC are externally mixed may introduce inaccuracy to our analysis. The C value is introduced and discussed in detail in the next section.

In summary, the good agreement between CAPS and SP2 measurements for DF and MGO provides us with confidence in the CAPS-measured b_{abn}. The poor agreement between the CAPS and AE33 data is attributable to a variable aerosol SSA. The poor agreement between the CAPS and MWAA requires a larger data set to understand, as the present sample size was limited and the MWAA-analyzed filters were very heavily loaded. Therefore, in the present analysis, we have chosen the CAPS data as the reference measurement of aerosol absorption. This choice means that our reported b_{abn}, $\mathrm{MAC}_{\mathrm{OM}}$, and k_{OM} are *conservative* values. As stated in the main manuscript, this conservative choice still results in reported values that are higher than previous literature reports.

S3 AE33 "C value"

In this section, we describe the calibration of the "C value" of the AE33, which we performed in order to expand the set of data for which MAC and k_{OM} could be calculated. The "C value" is the ratio of the AE33-measured wavelength-dependent light attenuation coefficient of a PM deposit on a filter, $b_{\mathrm{ATN},\lambda}$ with b_{abn},

$$b_{\mathrm{abn},\lambda} = \frac{b_{\mathrm{ATN},\lambda}}{\text{C-value}}. \tag{S3}$$

In Eq. S3 and in this supplement, we write "C value" rather than simply "C" to avoid confusion of the C-value with the concentrations (C_X) discussed in the main manuscript.

The C value is intended to account for the multiple scattering of light within the filter. In practice, the determination of the C value is not specific to that effect, but rather the C value is used as a general calibration factor to adjust the b_{abn} values measured by the AE33 to those of a reference instrument (here, the CAPS PMssa). Since the CAPS PMssa measurements in this study were performed at 780 nm, we first calculated C values at 780 nm. The potential wavelength dependence of these C values is discussed afterwards. Note that because we have not independently corrected for particle losses in our sampling lines, our calculated C values may reflect line losses between AE33 and CAPS PMssa to some degree (we estimate that this error is less than the uncertainties listed in the main manuscript). The CAPS PMssa, SP2, and AMS were adjacent to one another, so the line losses for these three instruments are considered to be identical and therefore implicitly corrected for in our analyses.

S3.1 C-value at 780 nm

Before discussing the results of our C value calculations, we note a difference between the values used in our calculations as compared to those used by *Drinovec et al.* [2015]. *Drinovec et al.* [2015] recommend an AE33 C value of 1.57 for atmospheric work. This value was calculated in combination with a $\mathrm{MAC}_{880\,\mathrm{nm,Drinovec}}$ of $7.77\,\mathrm{m}^2\,\mathrm{g}^{-1}$. In our analysis, we have taken the $\mathrm{MAC}_{880\,\mathrm{nm,Bond}}$ of $4.69\,\mathrm{m}^2\,\mathrm{g}^{-1}$ recommended by *Bond and Bergstrom* [2006] as a reference value, for which the C value comparable to 1.57 is 2.56 (a factor 1.63 larger, since $\mathrm{MAC}_{880\,\mathrm{nm,Bond}}$ is a factor 1.63 smaller than $\mathrm{MAC}_{880\,\mathrm{nm,Drinovec}}$).

In applying Eq. S3, we have used the CAPS-PMssa-measured b_{abn} and the AE33-measured b_{ATN}. For this calculation, it is necessary to convert the CAPS b_{abn} measurements at 780 nm to a wavelength used by the AE33, such as 880 nm using Equation 1. We used an AAE of 1 for this conversion, so that the analysis was consistent for all fuels. Fig. S12 shows the resulting C values, plotted against SSA following *Collaud Coen et al.* [2010]. The five highest-SSA measurements have been removed due to high uncertainty in the extinction-minus-scattering technique at high SSA (the 90 % confidence interval of the calculated C value was as large as its magnitude). Our confidence in the remaining SSA values is reinforced by the good correlation between CAPS-measured b_{abn} and SP2-measured rBC concentrations in Fig. S1, as noted above. The mean and SD of the determined C values (weighted by the uncertainties) are 4.7 ± 1.1. The median calculated C value is a factor 2.6 (median) higher than the reference value of 2.56, which corresponds to a factor 2.6 median reduction in b_{abn}. As noted above, a part of this reduction may be related to line losses. As this factor is greater than one, a significantly smaller absorption coefficient b_{abn} is obtained from a given value of attenuation coefficient b_{atn}. Our recalibration of the C value therefore results in conservative estimates of k_{OM} and brC MAC.

Since the SSA is not measured as commonly as chemical composition, we also note that the C value was correlated with the ratio $C_{\mathrm{BC}} : (C_{\mathrm{OM}} + C_{\mathrm{SO4}})$ (Fig. S13). This correlation, however, was much poorer than the correlation with SSA for the same reasons (discussed in the main manuscript) that no simple predictor could be found for the SSA.

S3.2 C-value wavelength dependence

A wavelength dependence in the C-value may arise due to the wavelength-dependent scattering of light by the AE33 filter fibers or due to the cross-sensitivity of the AE33 to light scattering by the sampled particles in the filter matrix. By comparison of our MWAA data (measured at five wavelengths, Fig. 6) with corresponding AE33 data (recall that the MWAA directly measures and corrects for scattering from the filter sample), we can directly conclude that the C-value wavelength dependence was negligible for HFO PM samples. MWAA data were not available for diesel or MGO samples. However, the AAE calculated from the AE33 data for these samples was close to 1.0, in agreement with extensive literature evidence for BC-dominated samples [*Bond et al.*, 2013]. Considering 1.0 as the true AAE of diesel and MGO PM, our measured AAE was accurate to 0.1, implying 10 % accuracy in the wavelength-dependence of our C-value.

Our conclusion that the AE33 C-value was negligibly dependent on wavelength is consistent with the conclusions of *Drinovec et al.* [2015]. Because one recent publication [*Segura et al.*, 2014] concluded otherwise for a different aethalometer model (the AE31), we provide further details on this topic here. The potential wavelength dependence of the C-value can be expressed in terms of two properties, namely a filter-property-dependent parameter $\mathrm{C}^*_{\mathrm{value}}$ and a fractional cross-sensitivity of the AE33 to aerosol scattering $m_s(\lambda)$. Although these two effects might not be completely independent, they have been treated as such in the literature [*Collaud Coen et al.*, 2010, and references therein]. These two terms are represented in the equation [*Segura et al.*, 2014]:

$$\mathrm{C}_{\mathrm{value}}(\lambda) = \mathrm{C}^*_{\mathrm{value}} + m_s(\lambda)\frac{\mathrm{SSA}(\lambda)}{1-\mathrm{SSA}(\lambda)}. \tag{S4}$$

Regarding the second term in this equation, *Drinovec et al.* [2015] measured $m_s(\lambda)$ as increasing with filter loadings with an asymptotic maximum value of 0.02 for 260 nm particles. For 160 nm particles, this maximum value was 0.01. In both cases, the dependence of $m_s(\lambda)$ on particle size was much greater than its dependence on measurement wavelength. Combining this value with the SSA measurements shown in Fig. 5, we used this equation to calculate that the $m_s(\lambda)$ term may lead to a bias in the AAE of $\ll 0.1$.

Regarding the first term in this equation, the influence of the filter property term $\mathrm{C}^*_{\mathrm{value}}$ can be tested by changing the filter material. Using two different filter materials with different scattering properties (as shown by differences in the $\mathrm{C}^*_{\mathrm{value}}$), *Drinovec et al.* [2015] in their Table 2b obtained consistent AAEs. We note that the $\mathrm{C}^*_{\mathrm{value}}$ (and therefore C-value, since $m_s(\lambda)$ is small) of the filter material which is used in the AE33 is the smaller of the two, indicating the smaller impact of the filter material on the results. While this is not a direct demonstration of the wavelength independence of $\mathrm{C}^*_{\mathrm{value}}$, it shows a minor dependence of such wavelength dependence on filter properties. In summary, the wavelength dependence of the C-value can be predicted to be minor, and this prediction is demonstrated by our MWAA measurements.

S4 Particle density

Particle densities were obtained both directly and indirectly. Direct measurements consisted of DMA–APM measurements as detailed in a previous publication [*Gysel et al.*, 2012]. The mobility size selected by the DMA is equivalent to the particle size for spherical particles. The mass-to-charge ratio selected by the APM is equivalent to the particle mass for singly-charged particles. Consequently, the particle density ρ_p can be estimated directly as $\rho_{p,\mathrm{direct}}$,

$$\rho_{p,\mathrm{direct}} = \frac{m_p}{V_p} = \frac{6m_p}{\pi d^3_{\mathrm{mobility}}} \tag{S5}$$

We emphasize that $\rho_{p,\mathrm{direct}}$ was only measured for the smaller particles in the size distribution (Fig. 3) due to statistical (too few particles at larger sizes) and experimental limitations (limited time was available for the measurements). Thus $\rho_{p,\mathrm{direct}}$ does not reflect the larger rBC particles.

Density was also estimated indirectly by comparing the mass fractions and literature-based densities of OM and sulfate, the dominant particulate constituents. The density of the sulfate component of the PM was taken as $1800\,\mathrm{kg\,m^{-3}}$, which is representative for both sulfuric acid ($\rho = 1840\,\mathrm{kg\,m^{-3}}$) and ammonium sulfate ($\rho = 1780\,\mathrm{kg\,m^{-3}}$). The density of the organic component of the PM was estimated from the elemental ratios obtained from the AMS mass spectrum using the parameterization proposed by *Kuwata et al.* [2012], the Kuwata density, $\rho_{p,\mathrm{K}}$. The volume-weighted average of these densities provides the particle density,

$$\rho_{p,\mathrm{AMS}} = f_{\mathrm{vol,OM}}\rho_{p,\mathrm{K}} + f_{\mathrm{vol,sulf}}\rho_{\mathrm{sulf}} \tag{S6}$$

Comparing $\rho_{p,\mathrm{K}}$ with $\rho_{p,\mathrm{direct}}$ allowed the following observations. We emphasize here that $\rho_{p,\mathrm{direct}}$ was measured for the smallest of the size modes only (Fig. 3), so that we interpret it as representing rBC-free particles:

- For MGO and DF, $\rho_{p,\mathrm{K}}$ showed a low bias of just 5 % and a standard deviation of 2 %. The low bias indicates that $\rho_{p,\mathrm{K}}$ was a reliable estimator of ρ_p for these two fuels. The low standard deviation indicates a consistent OM composition for these two fuels. This consistent composition is consistent with the conclusion of *Eichler et al.* [2017], that lubrication oil was the major source of OM in these cases. We note that the data used by *Kuwata et al.* [2012] to obtain the $\rho_{p,\mathrm{K}}$ parameterization used here included light hydrocarbons (as found in lubrication oil) and that the expected accuracy in this parameterization, given by those authors, is 12 %. We note also that *Corbin et al.* [2015] found good agreement between $\rho_{p,\mathrm{K}}$ and $\rho_{p,\mathrm{measured}}$ for wood-burning OM.
- For HFO, $\rho_{p,\mathrm{K}}$ was biased 50 % lower than $\rho_{p,\mathrm{direct}}$, and showed a weak dependence on engine load. The low bias and engine-load dependence indicate that either the $\rho_{p,\mathrm{K}}$ parameterization or Equation S6 was not applicable to the HFO PM. Further data are needed to understand this difference of OM properties in HFO and MGO.

S5 Extended discussion

S5.1 $\mathrm{MAC}_{\mathrm{OM},370\,\mathrm{nm}}$ and thermal–optical OC

Since significant variation between engine emissions in future studies is expected (due to engine and fuel variability) we sought a simple empirical relationship between $\mathrm{MAC}_{\mathrm{OM},370\,\mathrm{nm}}$ and an easily-measured quantity. In Fig. S5 we show such a relationship between $\mathrm{MAC}_{\mathrm{OM},370\,\mathrm{nm}}$ and OC3 / OC, where OC3 is defined from the IMPROVE-A thermal/optical protocol as the total carbon evolved between 280–480 °C in an inert atmosphere (over $\sim$ 4 minutes), and OC is the standard IMPROVE-A-reported organic carbon.

We omitted OC4 (carbon evolved at 480–580 °C) from the numerator of OC3 / OC to avoid a sensitivity of the results to our choice of the so-called "split point" between OC and EC. The results were not sensitive to this omission. Our intention here is for OC3 to represent the large aromatic molecules which have been measured to volatilize from HFO PM at this stage [*Streibel et al.*, 2017] and have been shown to be the major chromophores in wood smoke [*Lorenzo et al.*, 2017]. Although "loss" of OC to pyrolysis is very significant in OC3 and OC4 for HFO, we did not find an improvement in the reported relationship when including pyrolyzed carbon on the abscissa.

In Fig. S5, $\mathrm{MAC}_{\mathrm{OM},370\,\mathrm{nm}}$ tends towards an asymptotic value of $\sim 1.5\,\mathrm{m}^2\,\mathrm{g}^{-1}$ as OC3 / OC increases. We hypothesize that the dependence of $\mathrm{MAC}_{\mathrm{OM},370\,\mathrm{nm}}$ on OC3 / OC is related to the relative contribution of lubrication oil in HFO OM. *Eichler et al.* [2017] showed that lubrication oil is an important component of HFO (and MGO and DF) OM, and evaporates below 160 °C. This evaporation temperature corresponds to either OC1 or OC2. However, consistent with previous reports [*Streibel et al.*, 2017], we find that HFO PM also contains substantial amounts of OC3 and OC4 *Streibel et al.* [2017]. Therefore, lubrication oil is not the only organic component in HFO PM. As the relative contribution of lubrication oil to HFO OM approaches zero, the ratio OC3 / OC would approach an asymptotic value. This asymptotic value may reflect the HFO fuel itself, as HFO typically contains a distillate OM fraction [*Stout and Wang*, 2016], which would be observed as OC1 or OC2. This asymptotic value would also be influenced by chemical transformations of the fuel during combustion. We note that the two outliers at high OC3 fractions, which were measured at very-low engine loads and charge-air pressures, are not explained by our hypothesis. In general, this analysis shows that describing HFO OM in terms of lubrication oil provides an insufficient picture of brC absorption in HFO PM. Rather, an additional description of large, relatively-low-volatility compounds is necessary to address the substantial brC absorption in HFO PM.

S5.2 AAEs: comparison with previous measurements

In Fig. S9, we compare PM absorption results from the present study (measurements performed in 2014) to a previous study (*Mueller et al.* 2015, measurements performed in 2012). Both studies used HFO in a marine diesel engine. Two-wavelength AAEs, $\mathrm{AAE}_{\lambda_1,\lambda_2}$ (Eq. 1), are used for the comparison: since the AAE is based on a ratio of measurements at two wavelengths, it is less likely to be biased by instrumental inaccuracies. The AAE probability density functions were obtained by a standard Gaussian-kernel method, which allows an estimated uncertainty in the AAE measurements of $\Delta_{\mathrm{kernel}} = 0.2$ to be incorporated in the plot via the kernel width. All curves represent at least 30 minutes of one-minute averages.

In general, differences between the AAEs in Fig. S9 indicate either a difference in the mass fraction of brC relative to BC, or to a difference in the properties of the brC. In the case of the 2014 data, we infer that only the mass fraction of brC relative to BC changed with engine load (except at 11 % load), because $\mathrm{MAC}_{\mathrm{OM},370\,\mathrm{nm}}$ did not vary as a function of engine load (except at 11 % load; Fig. 7).

Roughly similar trends are seen for the two studies, with higher AAE(370,880) observed at 25 % compared to 75 % load. (The 91 % load data for 2014 are not included as only 8 measurements were available.) Lower engine loads always corresponded to higher AAEs, indicating the production of either more-absorbing brC or higher brC : eBC ratios at lower engine loads. The AAE(370,880) of DF appears to have been smaller in 2012 compared to 2014, possibly due to a change in the BC monomer size or compactness [*Scarnato et al.*, 2013].

When interpreting Fig. S9, it is essential to recognize that the engine used to combust HFO was very different between the two campaigns. Although both measurements were performed on the same HFO-ready diesel engine, the hardware of the engine was changed between 2012 and 2014. The engine operation was performance-optimized for HFO in both cases, which however means differences in fuel-injection speed and timing, charge air pressure, exhaust-gas back pressure, and compression ratio. Also, the HFO samples were also different between the campaigns and the engine load was allowed more time to equilibrate during the 2014 measurements. Therefore, while the two campaigns are best considered as representing two unrelated examples of the composition of HFO marine-diesel-engine emissions, they agree qualitatively.

S6 Aerosol Direct Radiative Forcing (DRF) estimation

Our simplified estimation of the impact of brC on DRF was based on the λ-resolved "simple forcing efficiency" defined by *Chen and Bond* [2010]:

$$\frac{d\mathrm{SFE}}{d\lambda} = \frac{1}{4}\frac{dS(\lambda)}{d\lambda}\tau_{\mathrm{atm}}^2(\lambda)\,(1-F_c)\,\left[2(1-a_s)^2\beta(\lambda)\cdot\mathrm{MSC}_{\mathrm{PM}}(\lambda) - 4a_s\cdot\mathrm{MAC}_{\mathrm{PM}}(\lambda)\right] \quad \text{(S7)}$$

where SFE is the simple forcing efficiency (W/g), S the solar irradiance, τ_{atm} the atmospheric transmission (0.79), F_c the mean cloud fraction, and β the backscatter fraction. The $\mathrm{MSC}_{\mathrm{PM}}$ and $\mathrm{MAC}_{\mathrm{PM}}$ are the mass scattering and absorption cross sections of the PM (not only of the BC or brC component).

We used an MSC of $2.3\,\mathrm{m}^2\,/\,\mathrm{g}$, calculated from our CAPS, SP2 and AMS measurements (mean b_{sca} divided by the mean total PM mass at 50 % load shown in Fig. S7). The SAE (scattering Ångström exponent, defined similarly to Eq. 1 but for $b_{\mathrm{scattering}}$) was assumed as 4 (the Rayleigh limit; *Moosmller et al.* 2009). Changing this value to 2 had a negligible effect on the results of the calculation.

We used the $\mathrm{MAC}_{\mathrm{BC}}$ and $\mathrm{MAC}_{\mathrm{OM}}$ measured at 50 % load and discussed in the main manuscript. In particular, we used the mean (fitted) $\mathrm{MAC}_{\mathrm{BC}}$ of $7.9\,\mathrm{m}^2\,/\,\mathrm{g}$ at $\lambda = 780\,\mathrm{nm}$ and an $\mathrm{AAE}_{\mathrm{BC}}$ of one to estimate $\mathrm{MAC}_{\mathrm{BC}}$. We used the λ-dependent $\mathrm{MAC}_{\mathrm{OM}}$ measured at 50 % load to estimate $\mathrm{MAC}_{\mathrm{OM}}$. We combined these MACs in a weighted average as

$$\mathrm{MAC}_{\mathrm{PM}} = f_{\mathrm{BC}} \cdot \mathrm{MAC}_{\mathrm{BC}} + f_{\mathrm{OM}} \cdot \mathrm{MAC}_{\mathrm{OM}} \tag{S8}$$

The fractions f_{BC} and f_{OM} are the measured mean mass fractions of BC and OM at 50 % engine load, which do not add up to zero for HFO (because 25 % of PM mass was sulfate; Fig. S8).

The surface albedo a was a free parameter and used to specify over-snow ($a = 0.7$) or over-ocean ($a = 0.06$) conditions [*Brandt et al.*, 2005]. Due to the simplicity of this model we did treated a as λ-independent.

To minimize the uncertainties associated with using a simple equation such as Eq. S7 to represent a system as complex as the earth, we reported relative DRFs only:

$$\Delta\mathrm{DRF}(\text{due to brC}) = \frac{\mathrm{SFE}(\text{BC+brC}) - \mathrm{SFE}(\text{BC-only})}{\mathrm{SFE}(\text{BC-only})} \tag{S9}$$

Where SFE(BC+brC) is the output of Eq. S8 with the inputs described above (representing the measurements) and SFE(BC-only) is the output of Eq. S8 with $\mathrm{MAC}_{\mathrm{OM}}$ set to zero (representing the null hypothesis that brown-carbon absorption in HFO PM is negligible).

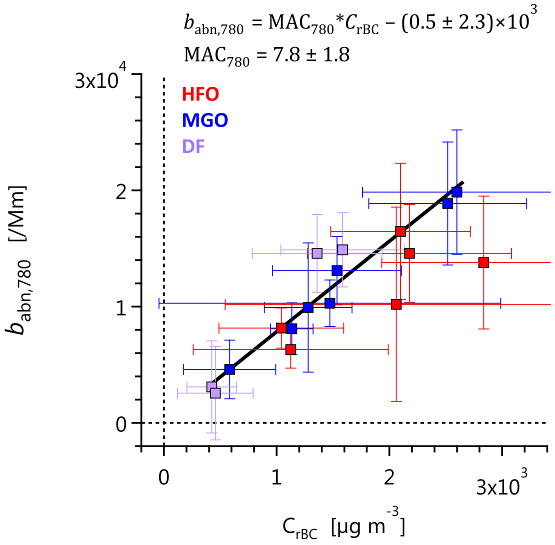

Figure S1. In-situ Mass Absorption Cross-section (MAC) of rBC at 780 nm for the three fuels, obtained from the SP2 and CAPS PMssa data. The MAC is given in units of μg m^{-3}. Data were fitted by weighted orthogonal distance minimization. Please note that these data represent a limited subset of engine loads (shown explicitly in Fig. 5) due to the limited availability of SP2 data. The two low-MAC outliers do *not* correspond to anomalous SP2 size distributions.

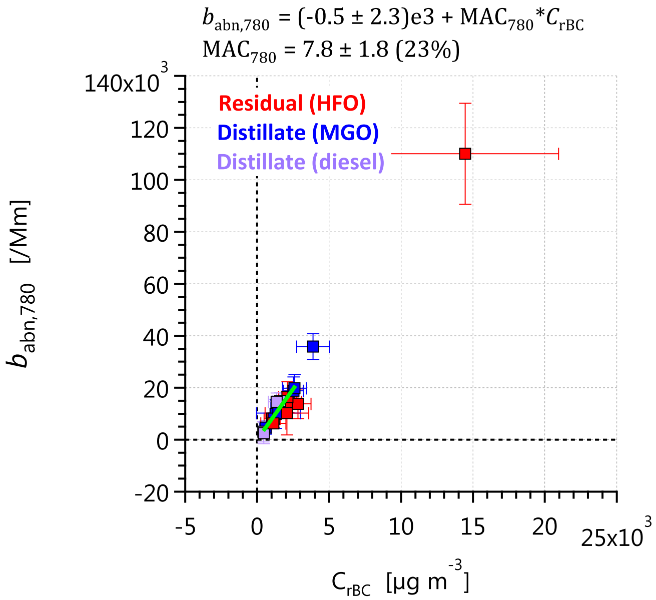

Figure S2. In-situ Mass Absorption Cross-section (MAC) of BC for the three fuels at 780 nm. Same in Fig. S1, but showing the two outliers that were excluded from the fit but included in Fig. 5. These outliers lie within the expected range.

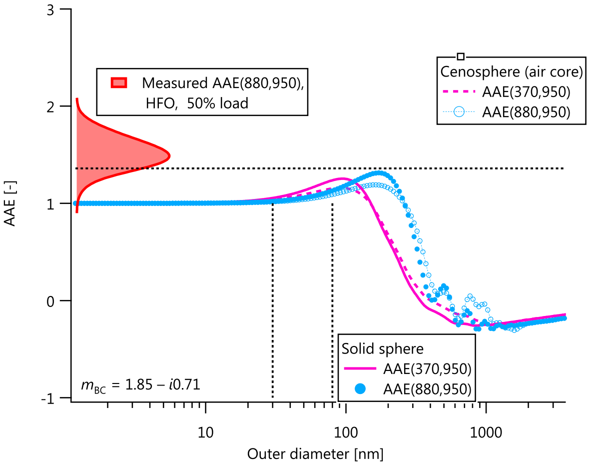

Figure S3. Comparison of measured AAE(880,950) with that predicted by Mie theory for two models of char particles: solid spheres and hollow cenospheres (*Huang et al.* [2012] showed that core-shell Mie theory provides an accurate model for cenospheres). Supermicron char particles have been observed by electron microscopy [*Bacci et al.*, 1983; *Chen et al.*, 2005]. These measurements show that the contribution of supermicron char particles to (AE33) absorption in our study was minor. Whereas the AAE of a supermicron char particle is roughly zero, the measured AAEs (from Fig. S9) are well above unity, indicating that the BC reaching the AE33 was generally soot or small char particles. The AAE(370,880) model results are included for context only.

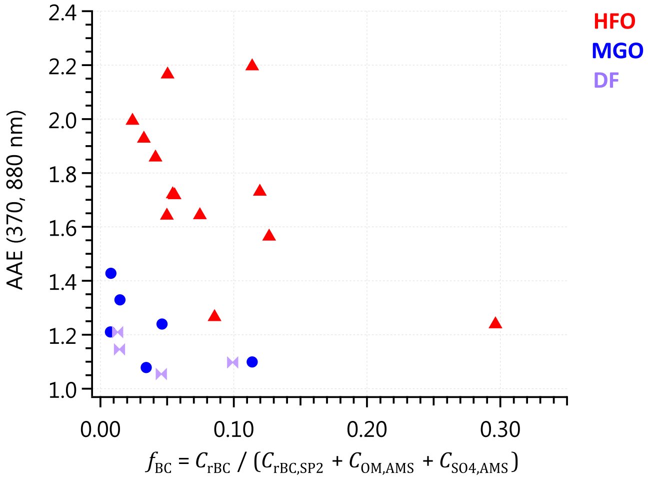

Figure S4. AAE(370, 880) as a function of the PM mass fraction of rBC f_{BC}, defined as shown in the graph. The trend of AAE(370, 880) with engine load is much stronger.

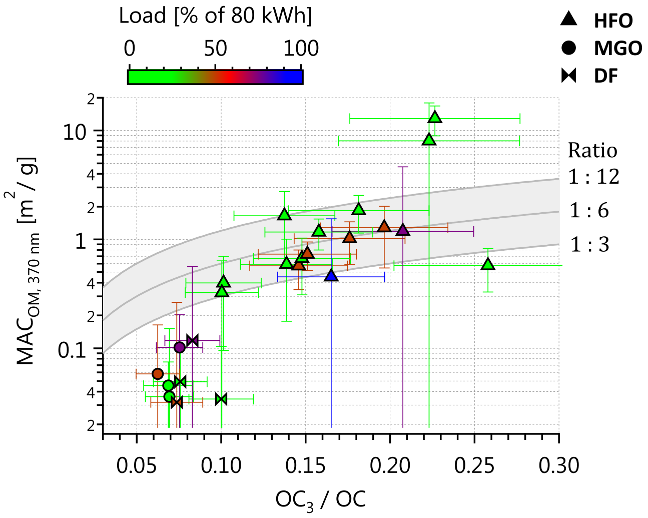

Figure S5. Scatterplot of $\mathrm{MAC_{OM,370\,nm}}$ and the fraction of OC3 in total thermal–optical (NIOSH) OC. The data are coloured by engine load for comparison with Fig. 7. Note that the two high-MAC outliers were measured at very low engine loads (standard engine operation is at 50 % load). The shaded lines show linear relationships of 1 : 3, 1 : 6, and 1 : 12.

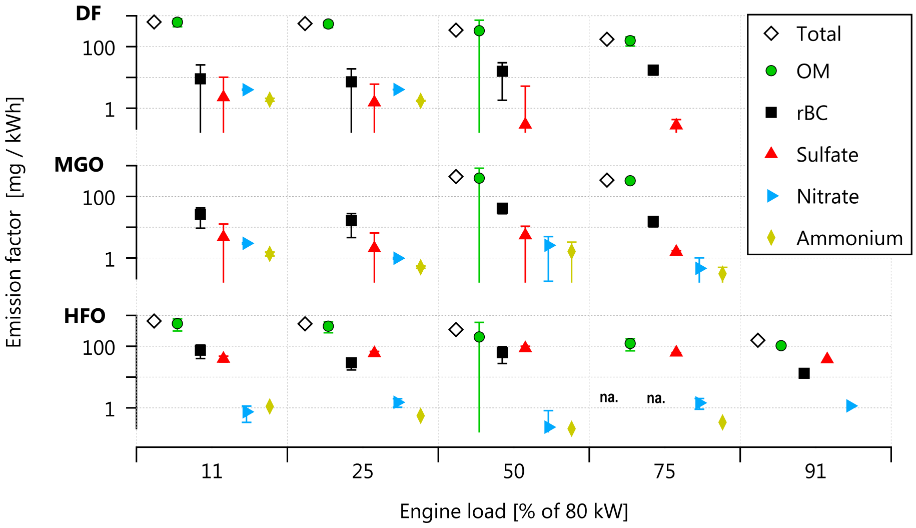

Figure S6. Emission factors for the three fuels and five engine loads. OM emissions dominated the total, contributing 90% of the mass for DF and MGO and 80% (< 50 % load) or 58 % (50% load) for HFO. HFO data for rBC at 75 % load, as well as MGO and DF data at 91 % load, were not available (n.a.). Note that the ordinate is on a log scale with minimum of 0.2 mg kWh^{-1} corresponding to the AMS detection limit at 91 % load (the detection limit is higher at lower loads).

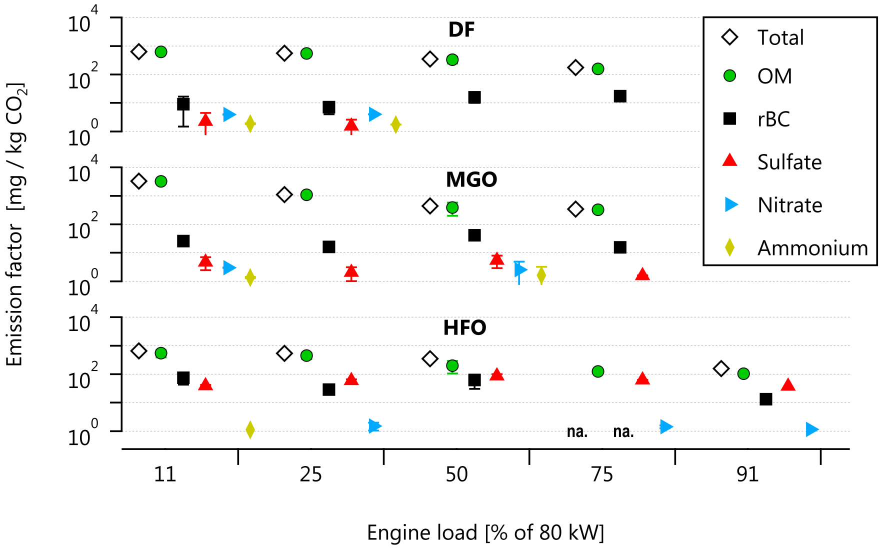

Figure S7. Engine-load-dependent emission factors for the three fuels. Same as Fig. S6 but normalized to CO_2.

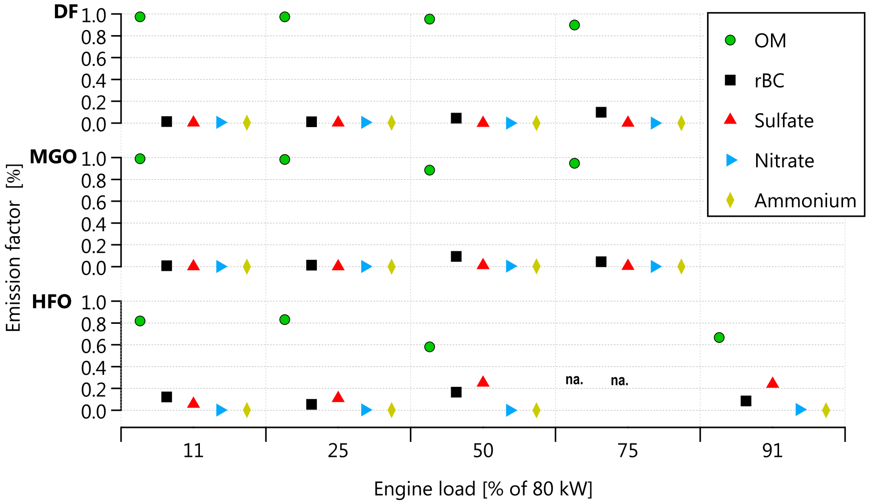

Figure S8. Engine-load-dependent emission factors for the three fuels. Same as Fig. S6 but expressed as percentage of the total measured mass.

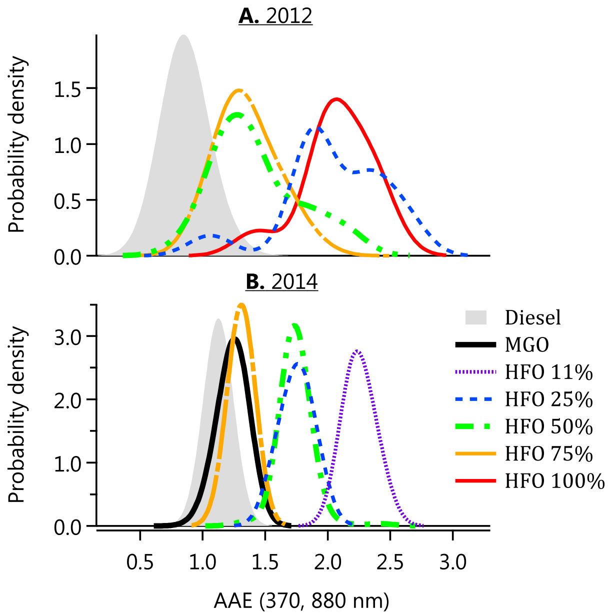

Figure S9. Absorption Ångström exponents (AAEs) probability distributions for the wavelength pair 370, 880 nm for a similar study performed in the year 2012 (**A**; *Mueller et al.* 2015) and for this campaign (**B**). The studies were performed on the same engine under two different configurations, with two different HFO fuel samples. The probability densities were obtained by a standard Gaussian-kernel method with kernel width estimated from the AAE uncertainty as $\Delta_{\text{kernel}} = 0.2$.

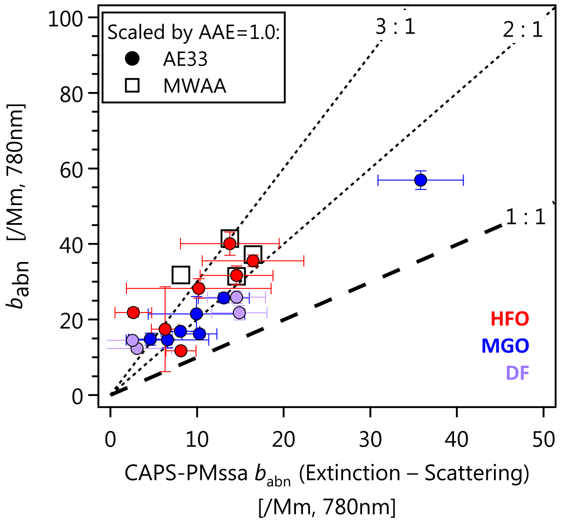

Figure S10. AE33 absorption and MWAA absorption plotted against absorption measured in situ by extinction minus scattering. In this plot, the AE33 absorption data have been analyzed using the factory-default C value (Section S3). It is important to realize that the MWAA and AE33 data are for different experiments. When plotted as a function of engine load, an inconsistency between the AE33 and MWAA results becomes apparent at higher loads (see Fig. S11 and its caption).

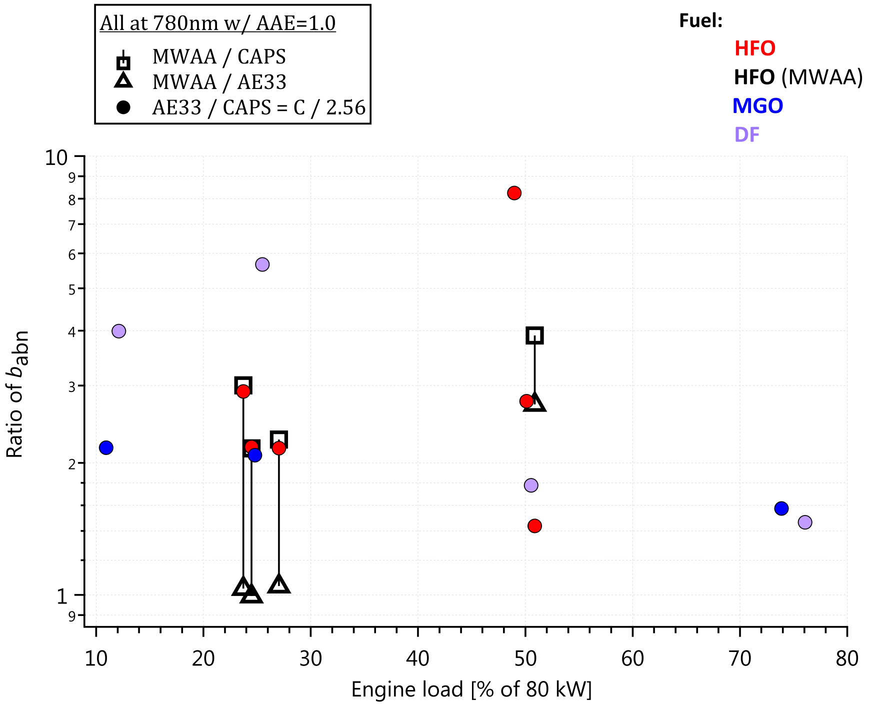

Figure S11. Ratios of absorption reported by MWAA (measured at 850 nm), AE33 (measured at 880 nm, calculated using the default C value of 2.56), and CAPS-PM$_{\text{SSA}}$. All MWAA data are for HFO; AE33 data are as labelled. Longer wavelengths were transformed to 780 nm-equivalent b_{abn} using an AAE of 1. Using an AAE of 1.7 (Fig. 6) would change these ratios by a factor of only 1.06 (MWAA) and 1.09 (AE33). Vertical blue lines indicate measurements of the same filter. Since only HFO data were analyzed by MWAA, this comparison should be interpreted with care: the anomalously large BC size distribution for HFO may have caused unexpected behaviour in all instruments.

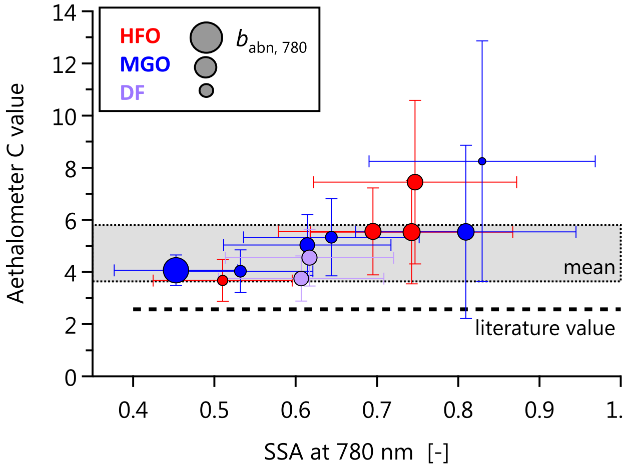

Figure S12. Relationship between AE33 C value (Eq. S3) and the single scattering albedo at 780 nm. The area of each symbol is scaled to $b_{\text{abn,780}}$. The weighted mean and SD are 4.7 ± 1.1.

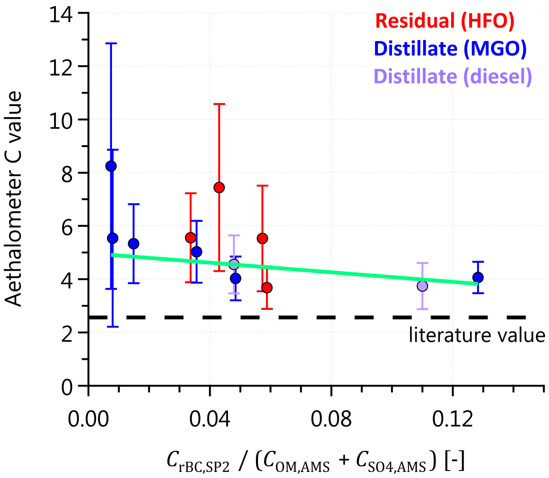

Figure S13. AE33 C value vs. the ratio of rBC to total PM (represented by the sum of OM and sulfate mass). The negative trend (slope −17 ± 8) suggests that higher C values were necessary to correct for increasingly important scattering artifacts at low rBC fractions, similar to Fig. S12. This plot (and fit) was not used in the present analysis due to a limited availability of C_{rBC} data and because of less scatter in Fig. S12.

References

Bacci, P., M. D. Monte, A. Longhetto, A. Piano, F. Prodi, P. Redaelli, C. Sabbioni, and A. Ventura (1983), Characterization of the particulate emission by a large oil fuel fired power plant, *J. Aerosol Sci.*, *14*(4), 557–572, doi:10.1016/0021-8502(83)90011-3.

Bond, T. C., and R. W. Bergstrom (2006), Light absorption by carbonaceous particles: An investigative review, *Aerosol Sci. Technol.*, *40*(1), 27–67, doi:10.1080/02786820500421521.

Bond, T. C., S. J. Doherty, D. W. Fahey, P. M. Forster, T. Berntsen, B. J. DeAngelo, M. G. Flanner, S. Ghan, B. Kärcher, D. Koch, S. Kinne, Y. Kondo, P. K. Quinn, M. C. Sarofim, M. G. Schultz, M. Schulz, C. Venkataraman, H. Zhang, S. Zhang, N. Bellouin, S. K. Guttikunda, P. K. Hopke, M. Z. Jacobson, J. W. Kaiser, Z. Klimont, U. Lohmann, J. P. Schwarz, D. Shindell, T. Storelvmo, S. G. Warren, and C. S. Zender (2013), Bounding the role of black carbon in the climate system: A scientific assessment, *J. Geophys. Res. Atmos.*, *118*, 5380–5552, doi:10.1002/jgrd.50171.

Brandt, R. E., S. G. Warren, A. P. Worby, and T. C. Grenfell (2005), Surface albedo of the antarctic sea ice zone, *Journal of Climate*, *18*(17), 3606–3622, doi:10.1175/jcli3489.1.

Chen, Y., and T. Bond (2010), Light absorption by organic carbon from wood combustion, *Atmos. Chem. Phys.*, *10*(4), 1773–1787.

Chen, Y., N. Shah, A. Braun, F. E. Huggins, and G. P. Huffman (2005), Electron microscopy investigation of carbonaceous particulate matter generated by combustion of fossil fuels, *Energy & Fuels*, *19*(4), 1644–1651, doi:10.1021/ef049736y.

Collaud Coen, M., E. Weingartner, A. Apituley, D. Ceburnis, R. Fierz-Schmidhauser, H. Flentje, J. Henzing, S. G. Jennings, M. Moerman, A. Petzold, O. Schmid, and U. Baltensperger (2010), Minimizing light absorption measurement artifacts of the aethalometer: evaluation of five correction algorithms, *Atmos. Meas. Tech.*, *3*, 457–474, doi:10.5194/amt-3-457-2010.

Corbin, J. C., A. Keller, B. Sierau, U. Lohmann, and A. A. Mensah (2015), Wood-stove and pellet-burner organic aerosol emissions aged in a continuous-flow photoreactor, *Aerosol Sci. Technol.*, *49*, 1037–1050, doi:10.1080/02786826.2015.1079586.

Corbin, J. C., A. A. Mensah, S. M. Pieber, J. Orasche, B. Michalke, M. Zanatta, H. Czech, D. Massabò, C. Buatier de Mongeot, C. Mennucci, I. El Haddad, N. K. Kumar, B. Stengel, Y. Huang, R. Zimmermann, A. S. H. Prévôt, and M. Gysel (2017), Trace metals in soot and pm$_{2.5}$ from heavy-fuel-oil combustion in a marine engine, *submitted to Environ Sci Technol*.

Drinovec, L., G. Močnik, P. Zotter, A. S. H. Prévôt, C. Ruckstuhl, E. Coz, M. Rupakheti, J. Sciare, T. Müller, A. Wiedensohler, and A. D. A. Hansen (2015), The" dual-spot" aethalometer: an improved measurement of aerosol black carbon with real-time loading compensation, *Atmos. Meas. Tech.*, *8*(5), 1965–1979, doi:10.5194/amt-8-1965-2015.

Eichler, P., M. Müller, C. Rohmann, B. Stengel, J. Orasche, R. Zimmermann, and A. Wisthaler (2017), Lubricating oil as a major constituent of ship exhaust particles, *Environ. Sci. Technol. Let.*, *4*(2), 54–58, doi:10.1021/acs.estlett.6b00488.

Gysel, M., M. Laborde, A. A. Mensah, J. C. Corbin, A. Keller, J. Kim, A. Petzold, and B. Sierau (2012), Technical note: The single particle soot photometer fails to reliably detect palas soot nanoparticles, *Atmos. Meas. Tech.*, *5*, doi: 10.5194/amt-5-3099-2012.

Huang, Y., R. Zhao, J. Jiang, and K.-Y. Zhu (2012), Scattering and absorptive characteristics of a cenosphere, *Int. J. Therm. Sci.*, *57*, 63–70, doi:10.1016/j.ijthermalsci.2012.01.019.

Kuwata, M., S. R. Zorn, and S. T. Martin (2012), Using elemental ratios to predict the density of organic material composed of carbon, hydrogen, and oxygen, *Environ. Sci. Technol.*, *46*(2), 787–794, doi:10.1021/es202525q.

Lorenzo, R. A. D., R. A. Washenfelder, A. R. Attwood, H. Guo, L. Xu, N. L. Ng, R. J. Weber, K. Baumann, E. S. Edgerton, and C. J. Young (2017), Molecular size separated brown carbon absorption for biomass burning aerosol at multiple field sites, *Environ. Sci. Technol.*, doi:10.1021/acs.est.6b06160.

Moosmller, H., R. Chakrabarty, and W. Arnott (2009), Aerosol light absorption and its measurement: A review, *Journal of Quantitative Spectroscopy and Radiative Transfer*, *110*(11), 844–878, doi:10.1016/j.jqsrt.2009.02.035.

Mueller, L., G. Jakobi, H. Czech, B. Stengel, J. Orasche, J. M. Arteaga-Salas, E. Karg, M. Elsasser, O. Sippula, T. Streibel, J. G. Slowik, A. S. H. Prévôt, J. Jokiniemi, R. Rabe, H. Harndorf, B. Michalke, J. Schnelle-Kreis, and R. Zimmermann (2015), Characteristics and temporal evolution of particulate emissions from a ship diesel engine, *Appl. Energy*, *155*, 204–217, doi:10.1016/j.apenergy.2015.05.115.

Müller, T., J. Henzing, G. De Leeuw, A. Wiedensohler, A. Alastuey, H. Angelov, M. Bizjak, M. C. Coen, J. Engström, C. Gruening, et al. (2011), Characterization and intercomparison of aerosol absorption photometers: result of two intercomparison workshops, *Atmos. Meas. Tech.*, doi:10.5194/amt-4-245-2011.

Petzold, A., and M. Schönlinner (2004), Multi-angle absorption photometry – a new method for the measurement of aerosol light absorption and atmospheric black carbon, *J. Aerosol Sci.*, *35*(4), 421–441, doi:10.1016/j.jaerosci.2003.09.005.

Scarnato, B., S. Vahidinia, D. Richard, and T. Kirchstetter (2013), Effects of internal mixing and aggregate morphology on optical properties of black carbon using a discrete dipole approximation model, *Atmos. Chem. Phys.*, *13*(10), 5089–5101, doi: 10.5194/acp-13-5089-2013.

Segura, S., V. Estellés, G. Titos, H. Lyamani, M. P. Utrillas, P. Zotter, A. S. H. Prévôt, G. Močnik, L. Alados-Arboledas, and J. A. Martínez-Lozano (2014), Determination and analysis of in situ spectral aerosol optical properties by a multi-instrumental approach, *Atmospheric Measurement Techniques*, *7*(8), 2373–2387, doi:10.5194/amt-7-2373-2014.

Stout, S., and Z. Wang (2016), *Standard Handbook Oil Spill Environmental Forensics: Fingerprinting and Source Identification*, 641–683 pp., Academic Press.

Streibel, T., J. Schnelle-Kreis, H. Czech, H. Harndorf, G. Jakobi, J. Jokiniemi, E. Karg, J. Lintelmann, G. Matuschek, B. Michalke, L. Müller, J. Orasche, J. Passig, C. Radischat, R. Rabe, R. Ahmed, C. Rüger, T. Schwemer, O. Sippula, B. Stengel, M. Sklorz, T. Torvela, B. Weggler, and R. Zimmermann (2017), Aerosol emissions of a ship diesel engine operated with diesel fuel or heavy fuel oil, *Environmental Science and Pollution Research*, p. 10976, doi:10.1007/s11356-016-6724-z.